20

Characteristics of the Laser-Induced Breakdown Detection of Colloidal Nanoparticles for Determining Particle Size

E.C. Jung and H.R. Cho
Nuclear Chemistry Research Division, Korea Atomic Energy Research Institute
Republic of Korea

1. Introduction

Laser-induced breakdown detection (LIBD) of colloidal nanoparticles has been investigated in various fields, such as the measurement of natural colloids in drinking water (Bundschuh et al., 2005; Kaegi et al., 2008; Wagner et al., 2005; Walther et al., 2006), the in-situ observation of colloid mediated pollutant transport (Hauser et al., 2002; Möri et al., 2003) and the real-time measurement of the solubility of radioactive elements (Bundschuh et al., 2000; Cho et al., 2008; Knopp et al., 1999; J.I. Kim, 2006; Neck et al., 2001, 2003; Opel et al., 2007; Walther et al., 2007). LIBD is an established technique that measures the size and concentration of colloidal particles in aqueous media using plasma formation, which is induced by focusing a short pulse laser beam into the solution (Kim & Walther, 2007). LIBD is especially efficient for detecting small particles less than 100 nm in diameter, which are not easily detectable using commercially available devices that adopt the measurement of a scattered light intensity, such as photon correlation spectroscopy (PCS) (Bundschuh et al., 2001b). Although several different LIBD systems have been developed over the last decades, a commercial instrument that adopts the LIBD method is currently unavailable.

This chapter is composed of a brief review of LIBD systems that adopt different detection schemes (Section 2), followed by the particle size determination methods (Section 3). Although these methods in principle allow the determination of particle size, until now, particle sizing capabilities in most LIBD experiments have been tested only for polystyrene reference particles with a well-defined size. Thus it should be verified that these LIBD methods are suitable for determining the particle size of different materials (Jung et al., 2011). Newly investigated characteristics of LIBD of colloidal uranium and alumina particles were reported in the last section (Section 4) followed by the summary (Section 5).

2. LIBD systems

In a recent publication, two different LIBD systems and their applications were reviewed in detail (Kim & Walther, 2007). One was based on the optical detection of plasma flash using either a photomultiplier tube (Ajiro et al., 1992; Fujimori et al., 1992) or a charge-coupled

device (CCD) camera (Bundschuh et al., 2001a, 2005; Hauser et al., 2002; Jung et al., 2006, 2007; J.W. Kim et al., 2008; Walther et al., 2002). A second system was based on the acoustic detection of a shock wave using a piezoelectric transducer (PZT) (Bundschuh et al., 2001b; Izumida et al., 1998; Kitamori et al., 1988, 1989; Satio et al., 1999; Scherbaum et al., 1996; Walther et al., 2004). Recently, we developed a modified LIBD system based on the optical detection of a shock wave; this system measures the deflection of a probe laser beam due to a shock wave-induced change in the refractive index of the liquid medium (Cho et al., 2008; Jung et al., 2009). In the next subsections, these different LIBD systems are described briefly based on the experimental apparatuses installed in our laboratory (Jung et al., 2006, 2007, 2009, 2011; Cho et al., 2008).

2.1 Optical detection of plasma flash using a CCD camera

A schematic diagram of the experimental arrangement of the LIBD system using a CCD camera is shown in Fig. 1 (Jung et al., 2006, 2007, 2011). The second harmonic (wavelength=532 nm, pulse width=6 ns, and pulse repetition rate=20 Hz) of the pulsed Nd:YAG laser (Continuum, Surelite II) was used for laser-induced breakdown. In order to adjust the laser beam diameter to approximately 4 mm, an iris diaphragm was installed on the travel path of the pulsed laser beam. Two Glan-Thompson polarizers, required to adjust the laser pulse energy, were arranged downstream of the iris diaphragm. The first polarizer was installed in such a fashion as to allow it to rotate; the second polarizer was installed to fix the direction so that only a polarized laser beam perpendicular to a bottom plane could pass through it. Accordingly, the laser pulse energy incident on the sample could be adjusted by rotating the first polarizer. The laser beam profile measured by a laser beam profiler (Newport, LBP-1) showed an approximately 80% Gaussian profile and the pulse-to-pulse fluctuation of the laser pulse energy was within 2.5% for 3,000 laser pulses. The laser beam was focused on the interior of a sample cell (Hellma, 111-QS) using a plano-convex

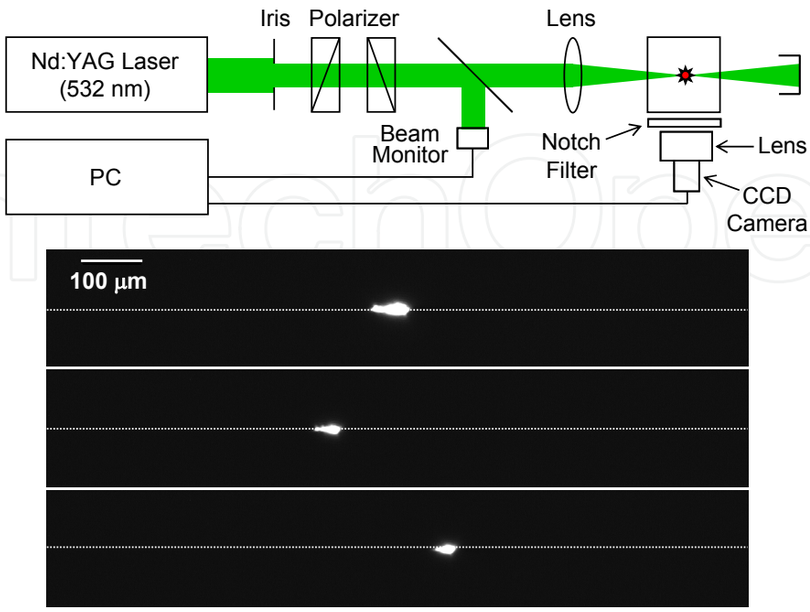

Fig. 1. Experimental setup and examples of plasma flashes acquired for each laser shot.

lens with a focal length of 40 mm. Laser-induced breakdowns occurred at the location on which the pulsed laser beam travelling in the *Z*-axis direction was focused.

The plasma flashes of the breakdown events were detected by a CCD camera (Hitachi Kokusai Electric, KP-F100BCL) with a variable macro-microscope. To prevent scattered laser light from reaching the CCD camera, a notch filter of ~1% transmission at 532 nm was inserted between the macro-microscope and the sample cell. Data from the CCD camera were recorded by a frame grabber card and processed by a home-made Labview software program. A typical example of the plasma flash is demonstrated in the lower part of Fig. 1, in which the optical image of a breakdown event is shown. The breakdown events occurred here and there along the laser beam propagation axis because of the Brownian motion of colloidal particles. In this study, the spatial distributions of 3,000 breakdown events were imaged on a pulse-to-pulse basis. A computer recorded the coordinates of plasma emission in the *X*-*Z* plane, the location and time of each breakdown event and the breakdown probability.

2.2 Acoustic detection of a shock wave using a PZT

A schematic diagram of the experimental arrangement of the LIBD system using a PZT is shown in Fig. 2. The role of each optical component was described in detail in previous subsection 2.1. When a laser-induced plasma is generated, a strong shock wave is propagated inside the liquid medium due to explosive expansion. To detect this shock wave, a PZT encapsulated in a cylindrical metal tube was attached to the wall of the sample cell. The coupling of metal tube housing to quartz sample cell was achieved by spiral springs. The waveform of the PZT signal was monitored using a digital oscilloscope (Tektronix TDS460A). The magnitude of the PZT signal was measured using a gated integrator (SRS SR250) and a boxcar averaging system (SRS SR280). The output was collected with a computer.

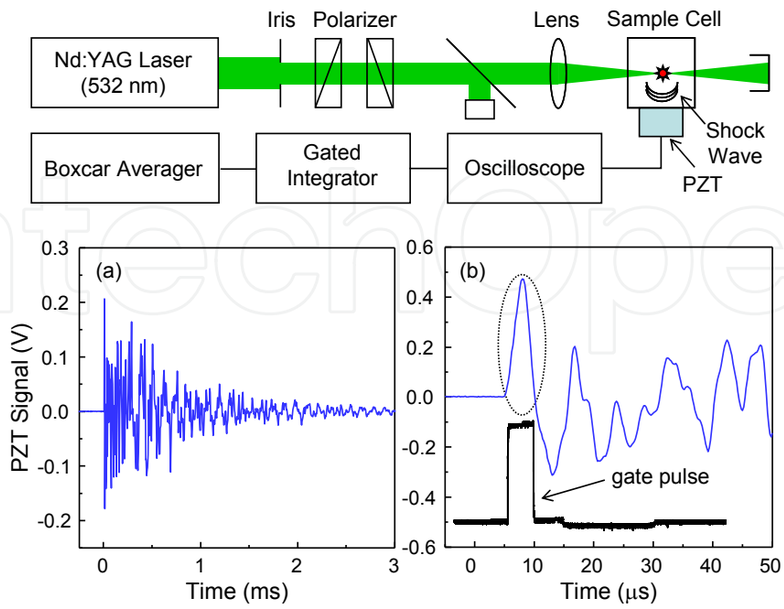

Fig. 2. Experimental setup and (a) PZT signal waveform acquired for a single laser shot, (b) early part of waveform (upper trace) and boxcar gate for signal detection (lower trace).

Fig. 2(a) and (b) shows the time trace as recorded by the PZT for a single laser shot and the early part of the waveform, respectively. The signal begins at a well-defined delay time t after the occurrence of the breakdown at $t = 0$, as shown in Fig. 2(b). This delay time was found to be linearly dependent on the distance between the focal point of the laser beam and the PZT surface. From these results, we are able to obtain a shock wave velocity of $\sim 1.48 \times 10^5$ cm/s. This is in good agreement with the established ultrasonic velocity at room temperature in water, which is $\sim 1.486 \times 10^5$ cm/s (Zapka et al., 1982).

In this experiment, the pulse height of the first signal in the waveform of the PZT signal, designated as a dotted circle in Fig. 2(b), showed a tendency to be proportional to the particle size (Kitamori et al., 1988, 1989). Thus the magnitude of the PZT signal was measured using a gated integrator with appropriate time delay and gate width as shown in the lower trace in Fig. 2(b). Because this signal magnitude was much higher than the magnitude of the electronic noise, each PZT signal magnitude greater than a certain threshold level was used to measure the breakdown event.

2.3 Optical detection of a shock wave using a probe beam

A schematic diagram of the experimental arrangement of the LIBD system using a probe beam is shown in Fig. 3 (Cho et al., 2008, Jung et al., 2009). The role of each optical component was described in detail in previous subsection 2.1. To detect the shock wave, a CW He-Ne laser (Uniphase, 20 mW) was used as a probe beam. When a laser-induced shock wave propagates through the medium, the refractive index of that medium changes. This change results in the deflection of the probe beam passing through the medium, and therefore the probe beam intensity reached at a high speed silicon photodiode (Thorlabs Det110) changes. A notch filter at 532 nm was used in order to prevent the photodiode from receiving the scattered light of the Nd:YAG laser. A pinhole (diameter of 0.5 mm) was used to detect the change in probe beam intensity for better sensitivity. The waveform of the probe beam signal was monitored using a digital oscilloscope (Tektronix TDS460A). The signal magnitude of the photodiode was measured using a gated integrator (SRS SR250) and a boxcar averaging system (SRS SR280). The output was collected with a computer.

Fig. 3(a) and (b) shows a typical waveform of a probe beam signal generated by a laser-induced shock wave and the early part of the waveform, respectively (Cho et al., 2008, Jung et al., 2009). The probe beam passed the 9.1 mm position below the focal point of the Nd:YAG laser beam, at which laser-induced breakdown occurred. The first peak at ~6.2 μs, which appears after the occurrence of the breakdown at $t = 0$, represents the deflected signal of the probe beam due to the shock wave. The second peak at ~9 μs results from the shock wave being reflected at the wall of the sample cell. The magnitude of the probe beam signal was measured using a gated integrator of appropriate time delay and gate width, as can be seen in the lower trace in Fig. 3(b). Comparing this technology with previously developed acoustic detection technology that used a PZT enables us to obtain a remote measurement in a non-contact manner. The probe beam signal begins at a well-defined delay time t after the occurrence of the breakdown at $t = 0$, as can be seen in Fig. 3(a) and (b). The delay time increases as the distance between the focal point of the laser beam and the probe beam position increases.

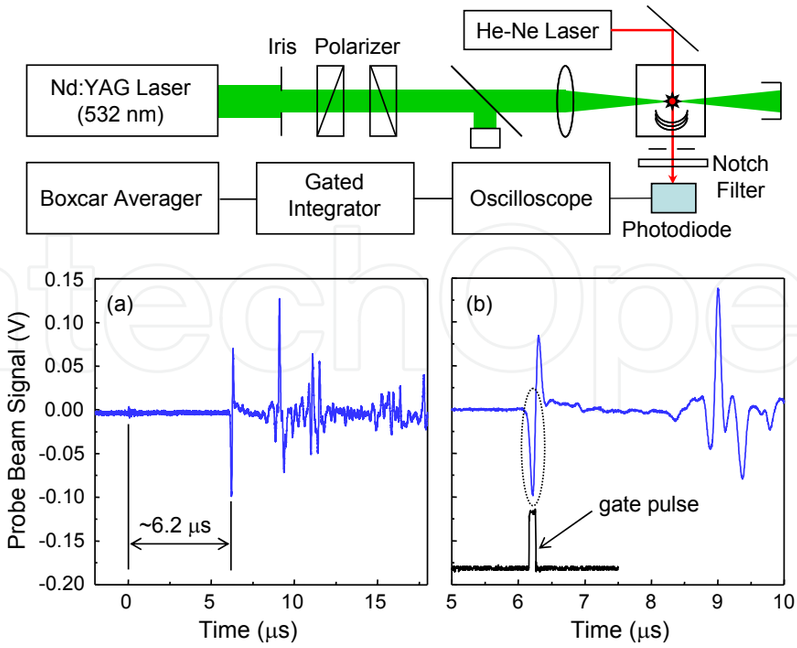

Fig. 3. Experimental setup and (a) probe beam signal waveform acquired for a single laser shot, (b) early part of waveform (upper trace) and boxcar gate for signal detection (lower trace).

Both a plasma emission and a shock wave can be measured simultaneously by constructing the detection components as shown in Fig. 4 (Jung et al., 2009). The laser beam propagated along the *Z*-axis direction was focused on an internal location of a sample cell. The probe beam propagated along the *Y*-axis direction passed by that location, which was lower than the focus of the pulsed laser beam by a distance "*d*" in the *X*-axis direction. By adjusting the distance downward from the focal point of the pulsed laser beam by approximately 12 mm, we were able to install the CCD camera and the PZT as can be seen in Fig. 4, to allow for simultaneous measurements.

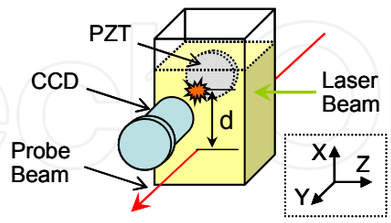

Fig. 4. Simultaneous detection using CCD camera, PZT and probe beam.

3. Particle size determination methods

The information on particle size is obtained by measuring the breakdown threshold energy which is defined as the minimum laser pulse energy required to generate a laser-induced plasma (Walther et al., 2002; Bundschuh et al., 2001a; Yun, 2007; Jung et al., 2011). The threshold energy can be determined from the breakdown probability measured as a function of the laser pulse energy (denoted as the "s-curve" in this chapter) (Walther et al.,

2002). Here, the breakdown probability is defined as the number of measured breakdown events divided by the total number of incident laser pulses.

Fig. 5 shows the breakdown probabilities as a function of the laser pulse energy for the 21 nm polystyrene particles at a laser wavelength of 532 nm. The empty and filled symbols represent the data derived from two different particle number densities, $5x10^8/cm^3$ and $5x10^7/cm^3$, for the same size particles. At a fixed particle number density, higher laser pulse energy resulted in higher breakdown probability. The threshold energy, corresponding to the laser pulse energy at which the breakdown probability is 0.01 in the s-curve, was determined in order to obtain the calibration curve for determining the particle size (Walther et al., 2002; Jung et al., 2011). At a fixed laser pulse energy, higher particle number density led to higher breakdown probability. As is apparent from the data shown in Fig. 5, the threshold energy is dependent on the particle concentration. In this study, the threshold energy was determined under experimental conditions in order to show that the increase in particle number density did not result in any further change of the threshold energy.

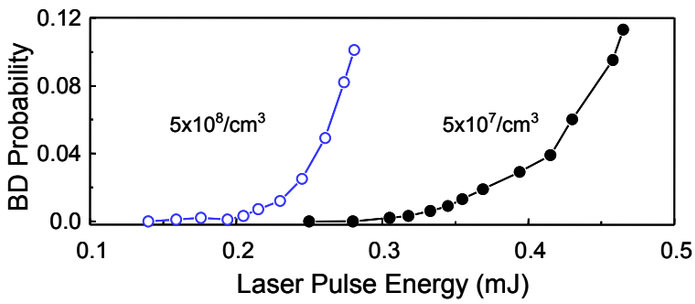

Fig. 5. Breakdown (BD) probability as a function of laser pulse energy for two different particle number densities. Data were obtained from polystyrene particles (size of 21 nm) at a laser wavelength of 532 nm.

Fig. 6 shows the dependence of the threshold energy on polystyrene particle size measured at a laser wavelength of 532 nm (Jung et al., 2011). At the fixed particle size, the threshold energy decreases with increasing particle number density, as depicted by the empty symbols in Fig. 6. The filled symbols indicate the minimum value of the threshold energy for each particle size. It is apparent that the threshold energy decreases with increasing particle size in this calibration curve.

The aforementioned particle sizing method, implemented by measuring the breakdown threshold energy, should be performed with a variation of the laser pulse energy. Under experimental conditions in which the laser pulse energy is fixed, the information on particle size can be obtained by measuring the spatial distribution of breakdown events (Bundschuh et al., 2001a; Hauser et al., 2002; Jung et al., 2007) and the frequency distribution curve of the magnitude of a laser-induced shock wave (Kitamori et al., 1989, Jung et al., 2009). In the next subsections, these methods are reported based on the experimental results obtained in our laboratory. In order to count only breakdown events induced by colloidal particles, the laser pulse energy was set to such a value that no breakdown event is observed in pure water.

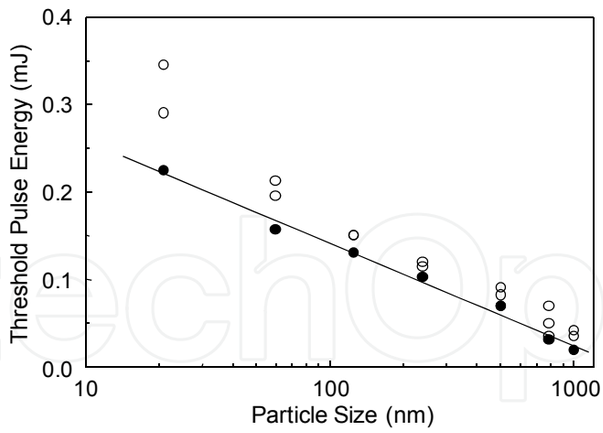

Fig. 6. Dependence of the breakdown threshold energies, which are defined as the energies at which the breakdown probability amounts to 0.01, on the particle size. Empty symbols represent the threshold energies determined from samples with different concentrations.

3.1 Particle sizing by measuring spatial distribution of breakdown events

The hyperbolic lines in Fig. 7 denote a focused laser beam propagated along the *Z*-axis; the spatial mode of the laser beam has a Gaussian profile with a beam waist of 5 μm at *Z*=0 (Jung et al., 2007). The exact focal point of the laser beam is designated as the origin of the coordinate axes. The contour lines in Fig. 7 represent the irradiance (equivalent to the power density) distribution of the laser beam. The regions indicated as "A" and "C" correspond to the upstream and downstream of the irradiance. The small ellipse indicated as "B" corresponds to the central region of the highest irradiance. As the laser beam waist increases along the *Z*-axis, the irradiance decreases, as depicted by the outer peanut-like shape.

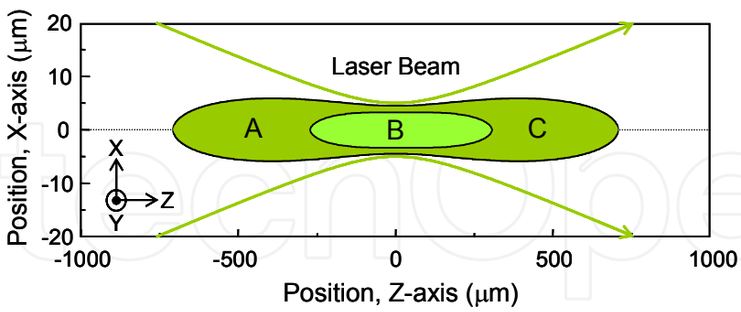

Fig. 7. Hyperbolic lines indicate the focused laser beam and contour lines indicate the laser irradiance distribution (A: upstream, B: central region of the highest irradiance, C: downstream).

When the CCD camera detects the plasma flash in the *X*-*Z* plane, as can be seen in Fig. 1, the spatial distribution of the breakdown events for small particles resembles the small ellipse shown in Fig. 7 because a breakdown is only induced at a region of a high irradiance, whereas the spatial distribution for large particles resembles the outer peanut-like shape due to their relatively low threshold energy for a breakdown (Bundschuh et al., 2001a).

Fig. 8 shows spatial distributions of 3,000 breakdown events for two different polystyrene particles (diameters of 21 nm and 60 nm) measured with a laser wavelength of 532 nm. Each data point represents the exact position on the *X*-*Z* plane at which a breakdown occurred. The length of the spatial distribution determined for 95% of the breakdown events (denoted the "effective focal length" in this manuscript) was measured in order to obtain the calibration curve for determining the particle size. At an incident laser pulse energy of 0.5 mJ, the breakdown probabilities were 0.2 for the 21 nm particles and 0.35 for the 60 nm particles, of which the concentrations were 1 parts per billion (ppb) and 7 ppb, respectively. The effective focal lengths were approximately 200 μm for the 21 nm particles and approximately 290 μm for the 60 nm particles. The spatial distributions of all data reported in this study exhibited good rotational symmetries centered on the origin of the *Z*-axis. Because the spatial distribution of the breakdown events along the *Z*-axis expands in proportion to a particle's diameter, a calibration for the particle sizing can be established by using these effective focal lengths (Bundschuh et al., 2001a).

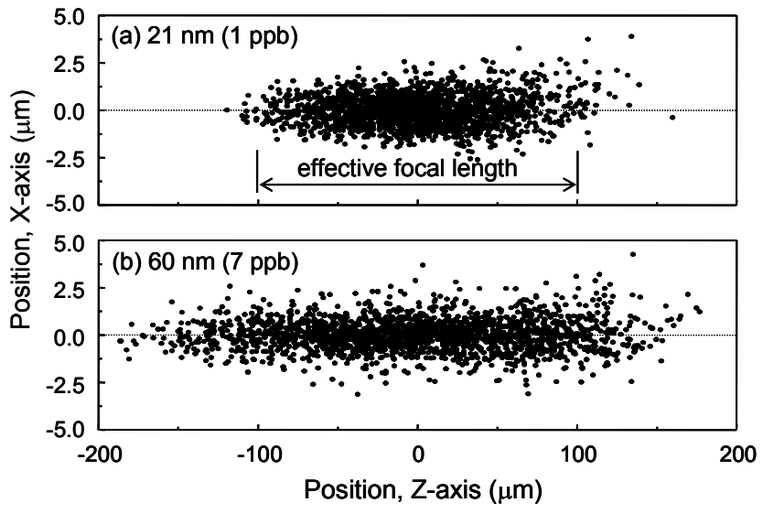

Fig. 8. Spatial distributions of 3,000 breakdown events for two different polystyrene particles (a) diameters of 21 nm (concentration of 1 ppb) and (b) 60 nm (concentration of 7 ppb). The length determined for the 95% of breakdown events was defined as the effective focal length.

3.2 Particle sizing by measuring frequency distribution of shock wave magnitude

Since each data point in Fig. 8 has its own acoustic signal magnitude, the main issue of this subsection is to investigate the size determination method by analyzing the acoustic signal magnitudes. Fig. 9 shows the distribution of PZT signal magnitude measured by the gated integrator and the boxcar averaging system, as explained in subsection 2.2. When a total of 3,000 laser pulses were incident to the sample cell containing the 21 nm polystyrene particles, 684 breakdown events, corresponding to a breakdown probability of 0.23, were measured. As is apparent from the data in Fig. 9, the signal magnitudes for the breakdown events were much higher (> 0.5 V) than the magnitude of the electrical noise of the PZT signal (< 0.2 V).

The frequency distribution curve of the PZT signal magnitudes, which were distributed in a wide voltage range, showed a Gaussian distribution, as plotted by solid line in Fig. 9. As an example of the frequency distribution curve, the data obtained from two different particles with diameters of 21 nm and 60 nm are shown in Fig. 10. Solid lines illustrate the Gaussian curves fitted to the experimental data points. The dependence of the peak and width of the distribution curve on the particle size is distinctive. The peak and width of the distribution curve increase as the particle size increases (Kitamori et al., 1989).

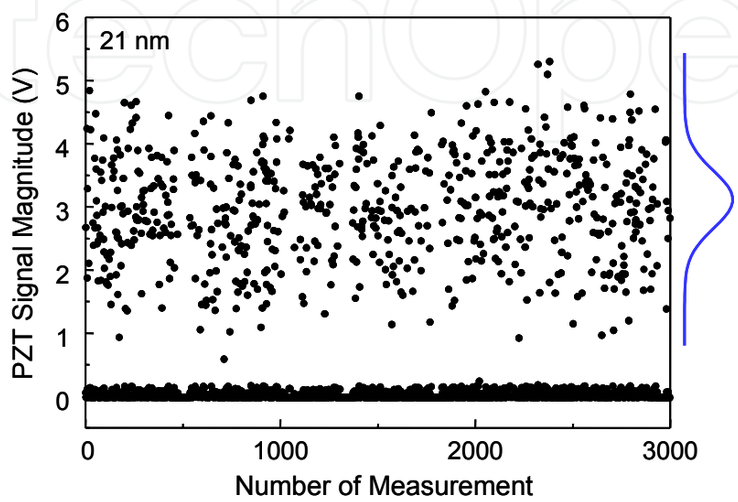

Fig. 9. Distribution of PZT signal magnitude for a total of 3,000 incident laser pulses.

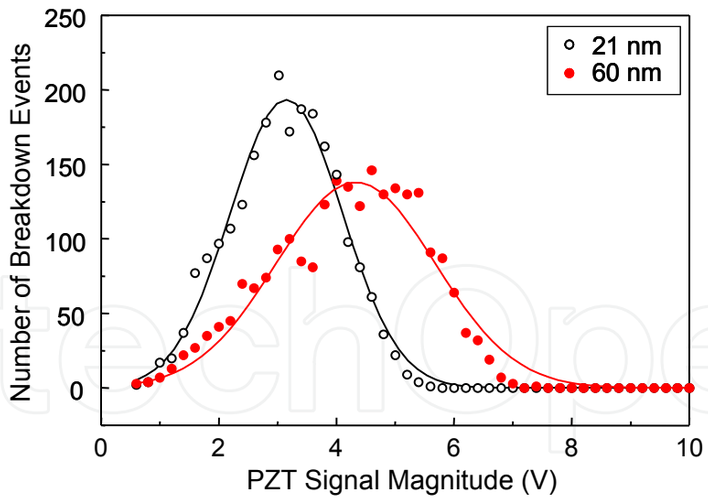

Fig. 10. The number of breakdown events as a function of the PZT signal magnitude for two different polystyrene particles (21 and 60 nm). Solid lines illustrate the Gaussian curves fitted to the experimental data points.

Although the detection method using PZT is very simple, this method has a drawback. It is difficult to obtain reproducible data due to the physical characteristics that are present when a PZT is directly attached to a sample cell to measure shock waves. Because several samples having particles of different sizes are contained in different sample cells, it is not easy to

firmly attach the PZT to each sample cell in exactly the same manner. Therefore, difficulty arises when the magnitudes of the PZT signals are compared with each other for a plurality of different sample cells (Jung et al., 2009).

Comparing the optical detection method using a probe beam with the acoustic detection method using a PZT, the former method is advantageous for detecting harmful colloidal particles (such as radioactive substances), which must be located in a special environment isolated from their surroundings (in a glove box or in a cleaning booth), because of its capability for remote measurement of a shock wave in a non-contact manner (Cho et al., 2008). At first, the effect of the particle size on the waveform of the probe beam signal was investigated. The pulse height and width of the first signal in the waveform, designated as a dotted circle in Fig. 3(b), were different for particles with different sizes (data not shown). It was observed that the pulse height and width increased as the particle size increased (Jung et al., 2009).

Fig. 11 shows the results obtained by measuring the frequency distribution of the probe beam signal magnitude with respect to standard polystyrene nanoparticles having different sizes under conditions in which the delay and width of the gate pulse were fixed, as can be seen in Fig. 3(b). The concentrations of the particles having sizes of 21, 33, and 60 nm were 1, 2 and 7 ppb, respectively. In Fig. 11, the *X*-axis denotes the magnitude of the probe beam signal; the *Y*-axis denotes the number of breakdown events of the respective polystyrene nanoparticles having different sizes. The interval of the *X*-axis during which the data was processed to form a frequency distribution curve is 0.1 V. As the size of the polystyrene nanoparticles increases, the peak of the frequency distribution curve increases. Therefore, the calibration curve required for the determination of the particle size can be obtained by using the peaks of different frequency distribution curves (Jung et al., 2009).

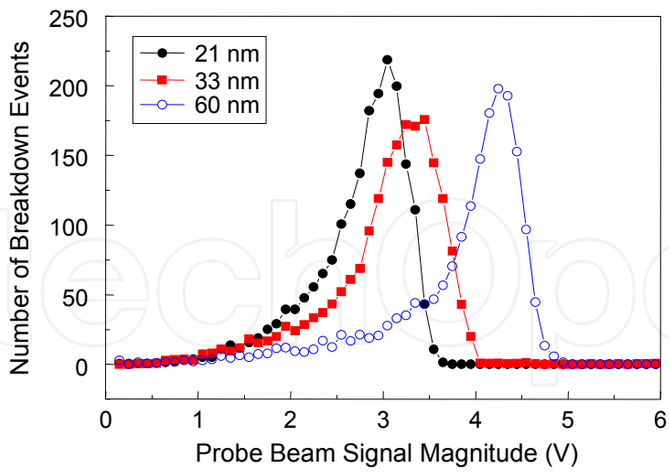

Fig. 11. The number of breakdown events as a function of the probe beam signal magnitude for three different polystyrene particles (21, 33 and 60 nm).

4. Material dependent characteristics of LIBD

Although the aforementioned LIBD methods in principle allow the determination of particle size, until now, particle sizing capabilities in most LIBD experiments have been tested only

for polystyrene reference particles with a well-defined size. Because physical processes such as multiphoton ionization (MPI) and electron cascade growth affect the generation of laser-induced plasma, characteristics of LIBD (the breakdown threshold energy in the s-curve, the spatial distribution of breakdown events and the frequency distribution curve of the shock wave magnitude) may appear in different ways for different materials having the same particle size. Thus, it should be verified that these LIBD methods are suitable for determining the particle size of different materials (Jung et al., 2011).

In this section, LIBD experiments were performed for several different materials: polystyrene, uranium, silica and alumina nanoparticles. Colloidal uranium particles are generated from a spent nuclear fuel, thus, the measurement of their sizes is of interest to understand their behavior in groundwater, to allow for the safety assessment of nuclear waste disposal. We were also motivated to examine the size of silica and alumina nanoparticles, which can form natural colloids in groundwater, because these colloidal particles serve as crucial carriers for the migration of radionuclides in groundwater.

4.1 Sample preparation

Monodisperse polystyrene (21, 33, 60, 125, 240, 500, 800 and 1000 nm, Duke Scientific), silica (60, 238, 490, 730 and 990 nm, Corpuscular and Duke Scientific) and alumina (50, 240, 500, 800 and 1080 nm, Corpuscular) particles of a well-defined size were used in this study. Before sample preparation, the company-certified particle sizes of these reference particles were confirmed once again in our laboratory by TEM (Transmission Electron Microscopy, Jeol Ltd., JEM-2000FXII) and PCS (Malvern, Zetasizer, Nano ZS90). These particles were suspended in ultra-pure water from a water purification apparatus (Millipore, Milli-Q-element).

For the uranium sample, a pure U(VI) solution in $HClO_4$ (Merck, analysis grade) was prepared from natural UO_2 powder dissolved in $HClO_4$. A U(VI) stock solution of 1.0 mM at pH 3.8 in 0.1 M $NaClO_4$ was prepared by addition of a 1.0 M NaOH solution (Sigma-Aldrich, 99.99% decarbonated NaOH) at room temperature (Cho et al., 2008; Jung et al., 2009). The stock solution was equilibrated with air for one year. The uranium concentration of the stock solution was determined by using a kinetic phosphorescence analyzer (Chemcheck, KPA-11). U(VI) samples were prepared in a glove box purged with Ar gas. An aliquot of the stock solution was slowly titrated with four different 0.1 M $NaClO_4$ solutions at pH levels of 3.8, 9, 10, and 11 to maintain the ionic strength of the samples at 0.1 M $NaClO_4$. The uranium concentration of each sample was calculated from the measured concentration of the stock solution and the dilution factor during titration. The basic solutions (pH 9, 10, 11) of 0.1 M $NaClO_4$ were prepared with 99.99% decarbonated NaOH (Sigma-Aldrich) in a glove box. For purification, $NaClO_4$:H_2O (Merck, analysis grade) was carefully recrystallized, diluted in pure water and filtered through a membrane filter (Advantec, mixed cellulose esters) with the pore size of 100 nm. By using LIBD system before the titration of the samples, it was proved that all the chemicals, including the uranium stock solution, contained no detectable colloidal particles. To minimize the adsorption of the formed uranium colloids on the surface of the test tubes, U(VI) samples were prepared in Teflon FEP tubes (Oak Ridge). U(VI) samples were equilibrated at 298±2 K during over one year in a glove box. The pH measurement was carried out with a glass combination pH electrode (Orion, Ross type, 6 mm diameter) calibrated with four pH buffer

solutions (Mettler Toledo, pH 2.00-9.21). For the size measurement of uranium colloidal particles, a portion of the uranium sample was delivered in a sealable quartz cell out of a glove box.

4.2 Particle sizing of uranium colloids with a laser wavelength of 532 nm

Fig. 12 shows the breakdown probability as a function of the pH of the uranium sample at the concentration of approximately 1 parts per million (ppm). The breakdown probabilities were almost zero below a pH value of 5.5, at which the given uranium concentration exceeded the solubility limit of U(VI) hydrolysis compounds. At a pH of 5.6 there was an observable increase in breakdown probability and uranium colloids were formed. After the onset of breakdown, the breakdown probability increased with the increase of the pH value. Using LIBD, we determined the mean particle size to be approximately 600 nm in the sample at a pH of 7.0 just after preparing the sample. In this experiment, the particle size of colloidal uranium was determined by using the calibration curve made from the effective focal length of the spatial distribution of breakdown events of polystyrene nanoparticles.

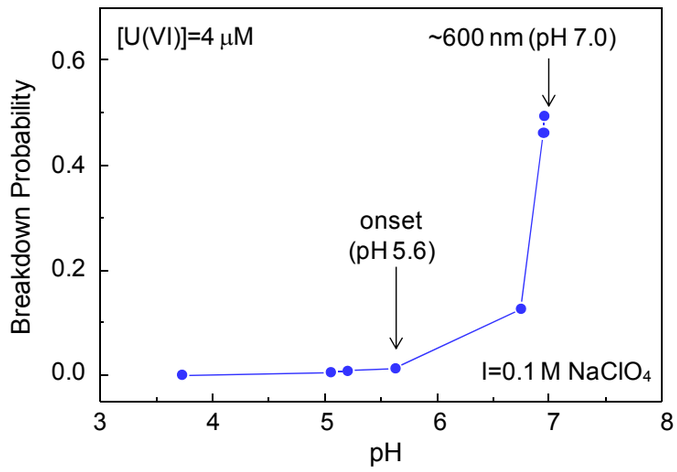

Fig. 12. Breakdown probability as a function of pH shows the formation of uranium colloidal particles.

One year after the sample preparation, the LIBD experiment was performed again to measure the size of the colloidal particles for the same sample. The solid symbol in Fig. 13 indicates the effective focal length obtained from the colloidal uranium particles, which were acidified to a pH of 5.8 after one year. When the effective focal length determined from the uranium sample was compared directly with the effective focal length values of the reference polystyrene particles, the mean particle size was found to be approximately 43 nm. From the change of the pH value from 7.0 to 5.8 and the change of the particle size from approximately 600 to 50 nm, we speculate that only small particles remained as suspended colloidal particles in the solution (Jung et al., 2009).

Because the characteristics of LIBD are dependent on not only the particle size but also the material properties, it is essential to compare the particle size determined using LIBD with the size determined using other methods, such as PCS and TEM. We tried to measure the particle size of uranium colloids, designated by the solid symbol in Fig. 13, using PCS, but

we could not measure the particle size of uranium colloids because of their extremely low concentration. For the purpose of comparison, we prepared another sample that showed a strong enough light scattering intensity of uranium particles for PCS (Jung et al., 2009). The supernatant of the uranium sample (1.0 mM of U(VI) at pH 6.12) was carefully concentrated by ultrafiltration using a cellulose filter (10 kD, Centrion YM-10, Millipore). The concentrated supernatant was collected in a sealable quartz cell.

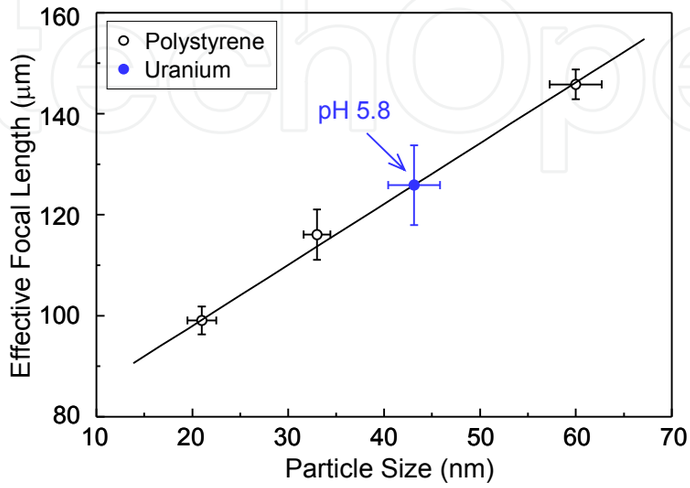

Fig. 13. Size measurement of colloidal uranium particles (solid symbol). The calibration curve was obtained from the effective focal lengths of the polystyrene reference particles with different sizes of 21, 33 and 60 nm in diameter (open symbols).

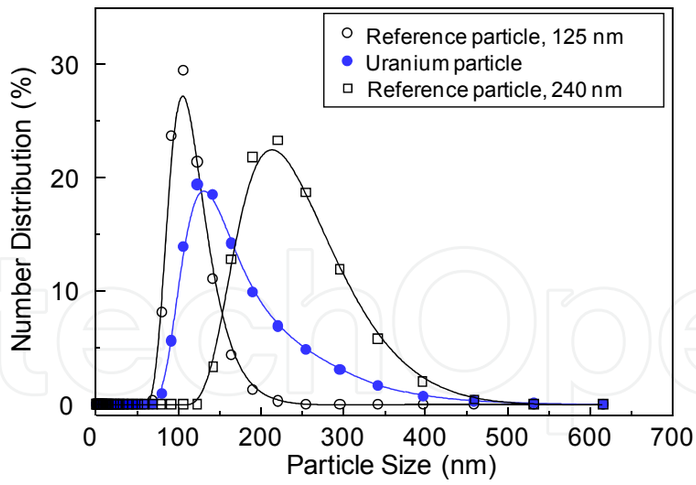

Fig. 14. Size measurement of colloidal uranium particles (solid symbol) and polystyrene reference particles (open symbols) using PCS.

The experimental number distributions for three different particles (two reference polystyrene samples and concentrated uranium sample) measured by PCS are presented in Fig. 14. The average sizes of the polystyrene particles were 143 and 257 nm with polydispersity indexes ranging from 0.05 to 0.08, respectively. Due to the hydrodynamic effect, these sizes were slightly larger than the sizes of 125 and 240 nm in diameter

determined by the manufacturer using TEM. The average size of uranium colloids in Fig. 14 was 210 nm with a polydispersity index of 0.15. The polydispersity index of uranium colloids, higher than those of reference particles, indicates the heterogeneity of uranium colloids in size and morphology. Nevertheless, the cumulated mean sizes obtained by repeating the experiments for one week were in the range of 205-215 nm (Jung et al., 2009).

A TEM image of colloidal uranium particles and the number-weighted particle size distribution from the TEM image analysis are shown in Fig. 15. The average size of the uranium colloids shown in Fig. 15 is approximately 200 nm, with a high polydispersity. Even though the shapes of the uranium particles are not ideal spheres, the average size of the uranium particles obtained from TEM is found to reasonably agree with the size determined by PCS.

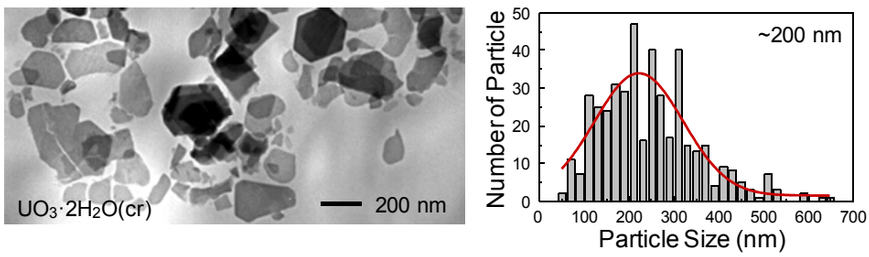

Fig. 15. TEM image of colloidal uranium particles and number-weighted particle size distribution obtained from TEM analysis.

Fig. 16 shows the particle sizes of concentrated uranium colloids determined by using the calibration curves made from the spatial distribution of 3,000 breakdown events for the reference polystyrene particles (21, 33, 60, 125 and 240 nm in diameter). The open and filled symbols in Fig. 16 represent the mean values obtained by repeating the experiments on the polystyrene and uranium particles, respectively. When the effective focal lengths determined in the uranium sample were compared directly with those of the reference particles, the estimated mean particle size was approximately 158 nm. Taking into account the polydispersity of the uranium colloids, the mean particle size determined using LIBD was in reasonable agreement with the sizes determined using PCS and TEM. Thus, we can obtain information on the relative differences or changes in the particle size of uranium colloids by using the present LIBD method (Jung et al., 2009).

To minimize the polydispersity of uranium particles, the large particles in the supernatant of the uranium sample were eliminated by filtration using a membrane filter (mixed cellulose ester, Advantec) having a pore size of 100 nm. The solid symbol designated by arrow in Fig. 16 represents the datum obtained from the filtrated sample. When the uranium datum was compared directly with the polystyrene data, the mean particle size of the filtrated uranium colloids was found to be approximately 31 nm. We tried to measure the particle size of the filtrated uranium colloids using PCS and TEM, but we could not measure the particle size of uranium colloids because of their extremely low concentration. Fig. 17 illustrates the spatial distributions of breakdown events for the same uranium particles as can be seen in Fig. 16. As is apparent from Fig. 17, the uranium colloids in the filtered sample show shorter effective focal length in the spatial distribution of breakdown events than that measured from the unfiltered, supernatant sample.

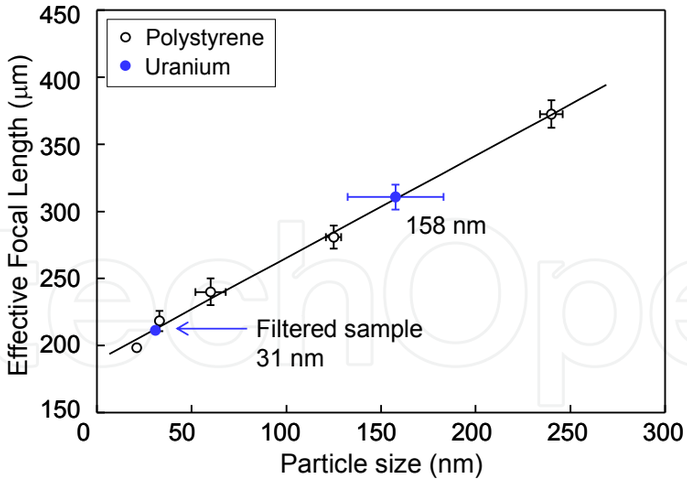

Fig. 16. Size measurements of colloidal uranium particles using effective focal lengths. The calibration curve was obtained from the size of the polystyrene reference particles having diameters of 21, 33, 60, 125 and 240 nm.

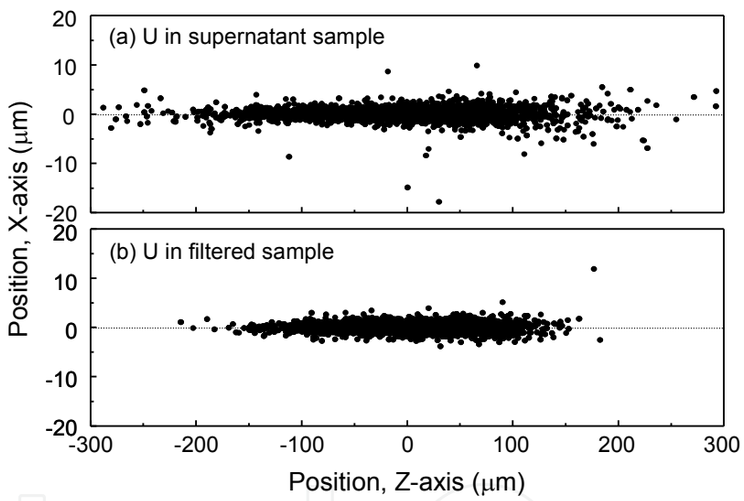

Fig. 17. Spatial distributions of 3,000 breakdown events for two different uranium particles in supernatant sample (a) and filtered sample (b).

4.3 Particle sizing of alumina colloids with a laser wavelength of 441 nm

Fig. 18 shows the effective focal lengths measured at a laser wavelength of 532 nm as a function of particle size for three different materials: polystyrene, silica and alumina colloidal particles. As already reported in the previous section, the effective focal length for polystyrene particles, designated as empty circles, is observed to be directly correlated to the particle size. In contrast, the effective focal lengths, designated as solid circles for alumina and square symbols for silica particles, are not correlated to the particle size. Although the solid lines fitted to the data points show slightly increasing behavior with poor correlation coefficients, it seems that the effective focal lengths for silica (Jung et al., 2011) and alumina are almost unchanged as the particle size increases.

The reason for these phenomena can be understood in terms of the difference in the ionization potentials (IPs) of these materials: ~7.8 eV for polystyrene, ~11.7 eV for silica and ~9.1 eV for alumina (Yun, 2007; Porter et al., 1955; B.H. Stephan, 1991). It is generally accepted that higher irradiance is required for the breakdown of a material with a higher IP. When a laser pulse at a wavelength of 532 nm (photon energy of ~2.33 eV) is used for the breakdown, simultaneous 4-photon absorption is required to induce MPI of polystyrene, while at least simultaneous 5-photon absorption is required for the MPI of silica and alumina. Thus, higher laser pulse energy is a prerequisite for the breakdown of silica and alumina, compared with that for polystyrene particles. It was reported that the breakdown threshold energy of silica was approximately 1.8-2.2 times higher than that of polystyrene particles (Bundschuh et al., 2001; Yun, 2007). The results shown in Fig. 18 imply that a size determination of silica and alumina particles using the spatial distribution of breakdown events measured at a laser wavelength of 532 nm is invalid under the present experimental conditions (Jung et al., 2011).

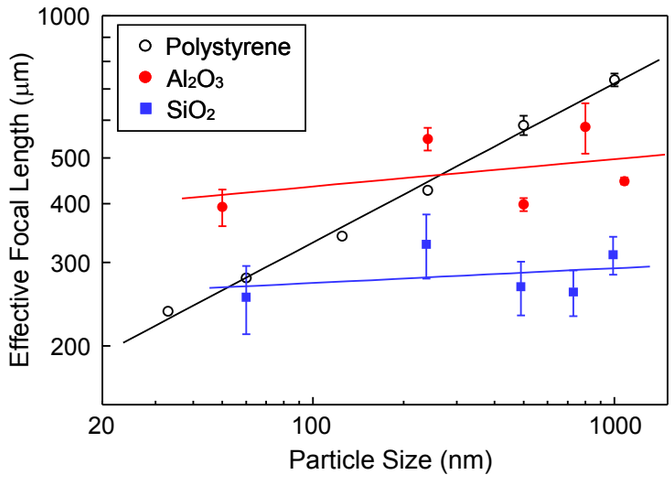

Fig. 18. Effective focal length as a function of particle size for polystyrene, silica and alumina particles at the laser wavelength of 532 nm.

As illustrated in Fig. 7, the irradiance distribution along the laser beam propagation axis can be divided into three distinct regions: the central region of highest irradiance near the focal point (region A), and the outside upstream and downstream regions of weak irradiance (regions B and C). The correlation between the effective focal length and the particle size for polystyrene reflects the fact that the breakdown of large particles is induced at the outside upstream and downstream regions, as well as at the central region, because the threshold energies of large particles are lower than those of small particles. The unchanged effective focal lengths for several silica and alumina particles indicate that breakdowns are only induced at the central region of high irradiance. It is speculated that these phenomena occur because the irradiance of the outside upstream and downstream regions is too low for breakdown, which requires simultaneous 5-photon absorption for the MPI (Jung et al., 2011).

The results shown in Fig. 19 illustrate the dependence of the effective focal length on the laser pulse energy, corroborating this speculation. Fig. 19 shows the effective focal length as

a function of laser pulse energy for polystyrene, silica and filtrated uranium particles. For polystyrene particles with different diameters (21, 33 and 60 nm), the effective focal length increases almost linearly with the increase of the laser pulse energy, ranging from 0.4 to 0.6 mJ. Similar to that of polystyrene particles, the effective focal length of filtrated uranium shows increasing behavior with increasing laser pulse energy. Our recent measurement of solubility product of U(VI) hydrolysis compounds suggests that the colloidal particles are $UO_3 \cdot 2H_2O$(cr) (Cho et al., 2008). The information on the IP of $UO_3 \cdot 2H_2O$(cr) particles is unknown at this time. However, under the assumption that the IP of $UO_3 \cdot 2H_2O$(cr) is not much different from the IP of UO_2 (IP=~6.17 eV) (Han et al., 2003), the MPI of the uranium compound can easily occur with 3- or 4-photon absorption at the photon energy level of ~2.33 eV. For silica (60 nm in diameter), however, the effective focal length does not change as the laser pulse energy increases, ranging from 0.5 to 0.6 mJ (Jung et al., 2011). With laser pulse energy above 0.6 mJ, breakdown occurs even for ultra-pure water.

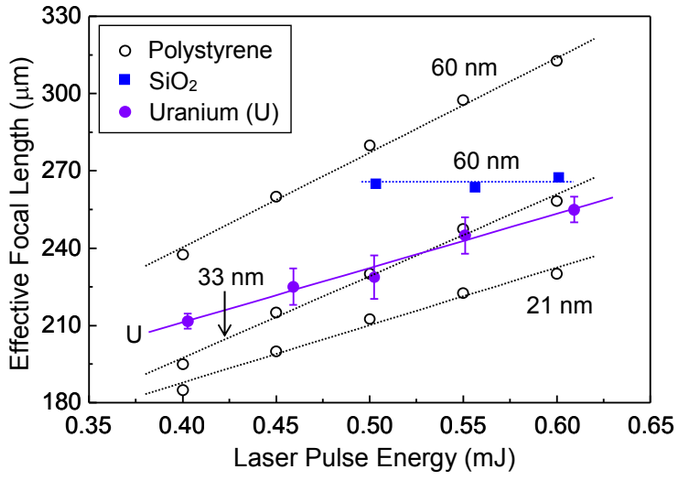

Fig. 19. Effective focal length as a function of laser pulse energy for polystyrene, uranium and silica particles at the laser wavelength of 532 nm.

When the laser photon energy is high enough, the MPI processes of silica and alumina may occur via simultaneous 4-photon absorption. As a result, breakdown events may occur in the upstream and downstream regions, as well as in the central region, because 4-photon absorption occurs at relatively low irradiance compared with 5-photon absorption. In this case, the correlation between the effective focal length in the spatial distribution of breakdown events and the particle size is expected even for silica and alumina particles.

To observe this effect, the dependence of the effective focal length on the particle size was investigated with a laser wavelength of 441 nm (photon energy of ~2.81 eV), and the results are shown in Fig. 20. It should be noted that the measurement of the incident wavelength-dependent characteristics of LIBD was performed by using a laser pulse generated from a wavelength tunable OPO (Optical Parametric Oscillator, OPOTEK, Vibrant) system. In this experiment, the OPO laser beam was focused on the interior of a sample cell using a bi-convex lens with a focal length of 15 mm. To prevent scattered laser light from reaching the CCD camera, a notch filter of ~1% transmission at 441 nm was inserted between the macro-microscope and the sample cell. When breakdown was

induced by 441 nm laser radiation, the 4-photon absorption energy of approximately 11.2 eV exceeded the IP of ~9.1 eV for alumina. Therefore, the dependence of the effective focal length on the particle size was obviously observed for alumina, which is designated as filled symbols in Fig. 20, as expected. More recently, the results on the calibration curve obtained with 355 nm laser radiation (photon energy of ~3.49 eV) was reported for silica particles and the similar dependence of the effective focal length on the particle size was observed (Jung et al., 2011).

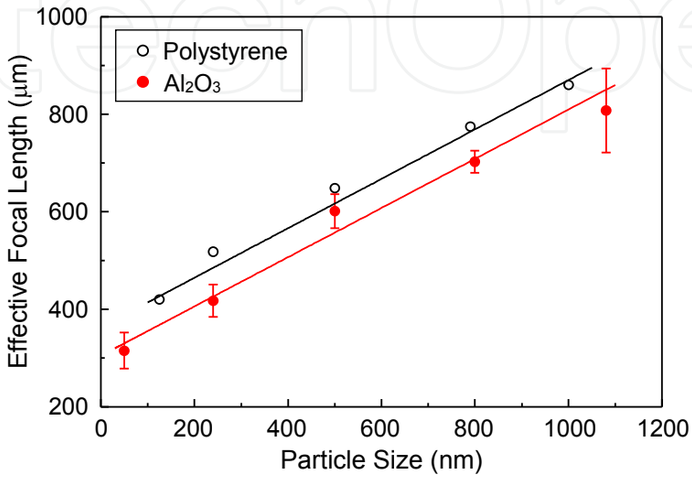

Fig. 20. Effective focal length as a function of particle size for polystyrene and alumina particles at the laser wavelength of 441 nm.

5. Summary

Several different LIBD systems using different detection devices, such as a PZT, a CCD camera and an optical probe beam, were described with their own particle size determination methods. In this chapter, material-dependent characteristics of LIBD were discussed for four different colloidal particles: polystyrene, $UO_3 \cdot 2H_2O$(cr), silica, and alumina. When a focused laser pulse of 532 nm wavelength is used to generate laser-induced plasma, simultaneous 4-photon absorption is required to induce MPI of polystyrene and $UO_3 \cdot 2H_2O$(cr); however, at least 5-photon absorption is required to induce MPI of silica and alumina. Thus, it was observed that the spatial distribution of the breakdown events measured with 532 nm laser radiation increased with increasing particle size for polystyrene and uranium compound, while spatial distribution of breakdown events was nearly unchanged for silica and alumina. The unchanged effective focal length with increase of particle size for silica and alumina resulted from the laser irradiance in the outside upstream and downstream regions, which was insufficient to induce MPI of these particles via simultaneous 5-photon absorption. When breakdown was induced by a laser wavelength of 441 nm, a correlation between the effective focal length and the particle size was observed for alumina because the simultaneous 4-photon absorption energy exceeds the IP of this material. Thus, the calibration curve obtained with an appropriate laser wavelength can be used to determine unknown particle sizes, even for materials with a high IPs.

6. Acknowledgment

This work was supported by the nuclear research and development program (2007-2011) through the National Research Foundation (NRF) of Korea funded by the Ministry of Education, Science and Technology (MEST). Part of this work was supported by the research and education program (2007) through the NRF of Korea funded by the MEST. The authors thank Mr. Hyungsoo Jung, Mr. Kilho Lee, and Mr. Sanghyun Park for obtaining data in section 3.1 and 3.2. The authors thank Ms. M.R. Park for obtaining data in section 4.3. The authors thank Dr. H.M. Kim for analyzing TEM results in section 4.2.

7. References

Ajiro, T.; Fujimori, H.; Matsui, T. & Izumi, S. (1992). Particle Size Dependence of Correlation Between Plasma Emission Delay Time and Plasma Emission Intensity of Laser Breakdown Induced by a Particle. *Japanese Journal of Applied Physics*, Vol. 31, No. 9, pp. 2760-2761, ISSN 0021-4922

Bundschuh, T.; Knopp, R.; Müller, R.; Kim, J.I.; Neck, V. & Fanghänel, Th. (2000). Application of LIBD to the Determination of the Solubility Product of Thorium(IV)-colloids. *Radiochimica Acta*, Vol. 88, No. 9-11, pp. 625-629, ISSN 0033-8230

Bundschuh, T.; Hauser, W.; Kim, J.I.; Knopp, R. & Scherbaum, F.J. (2001a). Determination of Colloid Size by 2-D Optical Detection of Laser Induced Plasma. *Colloids and Surfaces A: Physicochemical and Engineering Aspects*, Vol. 180, pp. 285-293, ISSN 0927-7757

Bundschuh, T.; Knopp, R. & Kim, J.I. (2001b). Laser-induced Breakdown Detection (LIBD) of Aquatic Colloids with Different Laser Systems. *Colloids and Surfaces A: Physicochemical and Engineering Aspects*, Vol. 177, pp. 47-55, ISSN 0927-7757

Bundschuh, T.; Wagner, T. U. & Koster, R. (2005). Laser-induced Breakdown Detection (LIBD) for the Highly Sensitive Quantification of Aquatic Colloids. Part I: Principle of LIBD and Mathematical Model. *Particle and Particle Systems Characterization*, Vol. 22, No. 3, pp. 172-180, ISSN 1521-4117

Cho, H.-R.; Jung, E.C. & Jee, K.Y. (2008). Probe Beam Detection of Laser-induced Breakdown for Measuring Solubility of Actinide Compounds. *Japanese Journal of Applied Physics*, Vol. 47, No. 5, pp. 3530-3532, ISSN 0021-4922

Fujimori, H.; Matsui, T.; Ajiro, T.; Yokose, K.; Hsueh, Y-M. & Izumi, S. (1992). Detection of Fine Particles in Liquids by Laser Breakdown Method. *Japanese Journal of Applied Physics*, Vol. 31, No. 5, pp. 1514-1518, ISSN 0021-4922

Han, J.; Kaledin, L.A.; Goncharov, V.; Komissarov, A.V.; Heaven, M.C. (2003). Accurate Ionization Potentials for UO and UO_2: A Rigorous Test of Relativistic Quantum Chemistry Calculations. *Journal of American Chemical Society*, Vol. 125, No. 24, pp. 7176-7177, ISSN 0002-7863

Hauser, W.; Geckeis, H.; Kim, J.I. & Fierz, Th. (2002). A Mobile Laser-induced Breakdown Detection System and Its Application for the in situ-monitoring of Colloid Migration. *Colloids and Surfaces A: Physicochemical and Engineering Aspects*, Vol. 203, 37-45, ISSN 0927-7757

Izumida, S.; Onishi, K. & Saito, M. (1998). Estimation of Laser-induced Breakdown Threshold of Microparticles in Water. *Japanese Journal of Applied Physics*, Vol. 37, No. 4, pp. 2039-2042, ISSN 0021-4922

Jung, E.C.; Yun, J.-I.; Kim, J.I.; Park, Y.J.; Park, K.K.; Fanghänel, Th. & Kim, W.H. (2006). Size Measurement of Nanoparticles Using the Emission Intensity Distribution of Laser-induced Plasma. *Applied Physics B*, Vol. 85, pp. 625-629, ISSN 0946-2171

Jung, E.C.; Yun, J.-I.; Kim, J.I.; Bouby, M.; Geckeis, H.; Park, Y.J.; Park, K.K.; Fanghänel, Th. & Kim, W.H. (2007). Measurement of Bimodal Size Distribution of Nanoparticles by Using the Spatial Distribution of Laser-induced Plasma. *Applied Physics B*, Vol. 87, pp. 497-502, ISSN 0946-2171

Jung, E.C.; Cho, H.-R.; Park, K.K.; Yeon, J.-W. & Song, K. (2009). Nanoparticle Sizing by a Laser-induced Breakdown Detection Using an Optical Probe Beam Deflection. *Applied Physics B*, Vol. 97, pp. 867-875, ISSN 0946-2171

Jung, E.C.; Cho, H.-R.; Park, M.R. (2011). Laser-Induced Breakdown Detection of Colloidal Silica Nanoparticles. Sumitted to *Applied Physics B*, ISSN 0946-2171

Kaegi, R.; Wagner, T.; Hetzer, B.; Sinnet, B.; Tzvekov, G. & Boller, M. (2008). Size, Number and Chemical Composition of Nanosized Particles in Drinking Water Determined by Analytical Microscopy and LIBD. *Water Research*, Vol. 42, pp. 2778-2786, ISSN 0043-1354

Kim, J.I. (2006). Significance of Actinide Chemistry for the Long-term Safety of Waste Disposal. *Nuclear Engineering and Technology*, Vol. 38, No. 6, pp. 459-482, ISSN 1738-5733

Kim, J.I. & Walther C. (2007). Laser-induced Breakdown Detection, In *Environmental Colloids and Particles: Behaviour, Separation and Characterisation*, Wilkinson, K.J. & Lead, J.R. (Ed.), pp. 555-612, Wiley, ISBN 978-0-470-02432-4, Chichester, U.K.

Kim, J.W.; Son, J.A.; Yun, J.-I.; Jung, E.C.; Park, S.H. & Choi, J.G. (2008). Analysis of Laser-induced Breakdown Images Measuring the Sizes of Mixed Aquatic Nanoparticles. *Chemical Physics Letters*, Vol. 462, No. 1-3, pp. 75-77, ISSN 0009-2614

Kitamori, T.; Yokose, K.; Suzuki, K.; Sawada, T. & Gohshi, Y. (1988). Laser Breakdown Acoustic Effect of Ultrafine Particle in Liquids and Its Application to Particle Counting. *Japanese Journal of Applied Physics*, Vol. 27, No. 6, pp. L983-L985, ISSN 0021-4922

Kitamori, T.; Yokose, K.; Sakagami, M. & Sawada, T. (1989). Detection and Counting of Ultrafine Particles in Ultrapure Water Using Laser Breakdown Acoustic Method. *Japanese Journal of Applied Physics*, Vol. 28, No. 7, pp. 1195-1198, ISSN 0021-4922

Knopp, R.; Neck, V. & Kim, J.I. (1999). Solubility, Hydrolysis and Colloid Formation of Plutonium(IV). *Radiochimica Acta*, Vol. 86, pp. 101-108, ISSN 0033-8230

Möri, A.; Alexander, W.R.; Geckeis, H.; Hauser, W.; Schäfer, T.; Eikenberg, J.; Fierz, T.; Degueldre, C. & Missana, T. (2003). The Colloid and Radionuclide Retardation Experiment at the Grimsel Test Site: Influence of Bentonite Colloids on Radionuclide Migration in a Fractured Rock. *Colloids and Surfaces A: Physicochemical and Engineering Aspects*, Vol. 217, No. 1-3, pp. 33-47, ISSN 0927-7757

Neck, V.; Kim, J.I.; Seidel, B.S.; Marquardt, C.M.; Dardenne, K.; Jensen, M.P. & Hauser, W. (2001). A Spectroscopic Study of the Hydrolysis, Colloid Formation and Solubility of Np(IV). *Radiochimica Acta*, Vol. 89, No. 7, pp. 439-446, ISSN 0033-8230

Neck, V.; Altmaier, M.; Müller, R.; Bauer, A. & Fanghänel, Th. (2003). Solubility of Crystalline Thorium Dioxide. *Radiochimica Acta*, Vol. 91, No. 5, pp. 253-262, ISSN 0033-8230

Opel, K.; Weiss, S.; Hübener, S.; Zänker, H. & Bernhard, G. (2007). Study of the Solubility of Amorphous and Crystalline Uranium Dioxide by Combined Spectroscopic Methods. *Radiochimica Acta*, Vol. 95, No. 3, 143-149, ISSN 0033-8230

Porter, R.F.; Chupka, W.A. & Inghram, M.G. (1955). Mass Spectrometric Study of Gaseous Species in the Si-SiO_2 System. *The Journal of Chemical Physics*, Vol. 23, pp. 216-217, ISSN 0032-9606

Saito, M.; Izumida, S.; Onishi, K. & Akazawa, J. (1999). Detection Efficiency of Microparticles in Laser Breakdown Water Analysis, *Journal of Applied Physics*, Vol. 85, No. 9, pp. 6353-6357, ISSN 0021-8979

Scherbaum, F.J.; Knopp, R. & Kim, J.I. (1996). Counting of Particle in Aqueous Solutions by Laser-induced Photoacoustic Breakdown Detection. *Applied Physics B*, Vol. 63, pp. 299-306, ISSN 0946-2171

Stephan, B.H.; Stephen, W.M. (1991). Determination of the Ionization Potentials of Aluminum Oxides via Charge Transfer. *The Journal of Physical Chemistry*, Vol. 95, No. 23, pp. 9091-9094, ISSN 0022-3654

Wagner, T. U.; Bundschuh, T. & Koster, R. (2005). Laser-induced Breakdown Detection (LIBD) for the Highly Sensitive Quantification of Aquatic Colloids. Part II: Experimental Setup of LIBD and Applications. *Particle and Particle Systems Characterization*, Vol. 22, No. 3, pp. 181-191, ISSN 1521-4117

Walther, C.; Bitea, C.; Hauser, W.; Kim, J.I. & Scherbaum, F.J. (2002). Laser Induced Breakdown Detection for the Assessment of Colloid Mediated Radionuclide Migration. *Nuclear Instruments and Methods in Physics Research B*, Vol. 195, pp. 374-388, ISSN 0168-583X

Walther, C.; Cho, H.-R. & Fanghänel, Th. (2004). Measuring Multimodal Size Distributions of Aquatic Colloids at Trace Concentrations. *Applied Physics Letters*, Vol. 85, No. 26, pp. 6329-6331, ISSN 0003-6951

Walther, C.; Büchner, S.; Filella, M. & Chanudet, V. (2006). Probing particle Size Distributions in Natural Surface waters from 15 nm to 2 mm by a Combination of LIBD and Single-particle Counting. *Journal of Colloid and Interface Science*, Vol. 301, No. 2, pp. 532-537, ISSN 0021-9797

Walther, C.; Cho, H.-R.; Marquardt, C.M.; Neck, V.; Seibert, A.; Yun, J.-I. & Fanghänel, Th. (2007). Hydrolysis of Plutonium(IV) in Acidic Solutions: No Effect of Hydrolysis on Absorption-spectra of Mononuclear Hydroxide Complexes. *Radiochimica Acta*, Vol. 95, No. 1, pp. 7-16, ISSN 0033-8230

Yun, J.-I. (2007). Material Dependence of Laser-induced Breakdown of Colloidal Particles in Water. *Journal of the Optical Society of Korea*, Vol. 11, No. 1, pp. 34-39, ISSN 1226-4776

Zapka, W.; Tam, A.C. (1982). Photoacoustic pulse generation and probe-beam deflection for ultrasonic velocity measurements in liquids. *Applied Physics Letters*, Vol. 40, No. 4, pp. 310-312, ISSN 0003-6951

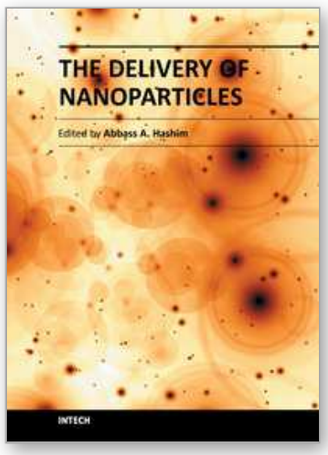

The Delivery of Nanoparticles
Edited by Dr. Abbass A. Hashim

ISBN 978-953-51-0615-9
Hard cover, 540 pages
Publisher InTech
Published online 16, May, 2012
Published in print edition May, 2012

Nanoparticle is a general challenge for today's technology and the near future observations of science. Nanoparticles cover mostly all types of sciences and manufacturing technologies. The properties of this particle are flying over today scientific barriers and have passed the limitations of conventional sciences. This is the reason why nanoparticles have been evaluated for the use in many fields. InTech publisher and the contributing authors of this book in nanoparticles are all overconfident to invite all scientists to read this new book. The book's potential was held until it was approached by the art of exploring the most advanced research in the field of nano-scale particles, preparation techniques and the way of reaching their destination. 25 reputable chapters were framed in this book and there were alienated into four altered sections; Toxic Nanoparticles, Drug Nanoparticles, Biological Activities and Nano-Technology.

INTECH
open science | open minds

InTech Europe
University Campus STeP Ri
Slavka Krautzeka 83/A
51000 Rijeka, Croatia
Phone: +385 (51) 770 447
Fax: +385 (51) 686 166
www.intechopen.com

InTech China
Unit 405, Office Block, Hotel Equatorial Shanghai
No.65, Yan An Road (West), Shanghai, 200040, China
中国上海市延安西路65号上海国际贵都大饭店办公楼405单元
Phone: +86-21-62489820
Fax: +86-21-62489821

IntechOpen